Inorganic Chemistry
Article
pubs.acs.org/IC

Two New Arsenides, $Eu_7Cu_{44}As_{23}$ and $Sr_7Cu_{44}As_{23}$, With a New Filled Variety of the $BaHg_{11}$ Structure

Dmitri O. Charkin,[†] Roman Demchyna,[‡,§] Yurii Prots,[§] Horst Borrmann,[§] Ulrich Burkhardt,[§] Ulrich Schwarz,[§] Walter Schnelle,[§] Igor V. Plokhikh,[†] Sergey M. Kazakov,[†] Artem M. Abakumov,[†,∥] Dmitry Batuk,[∥] Valery Yu. Verchenko,[†,⊥] Alexander A. Tsirlin,[⊥] Caroline Curfs,[#] Yuri Grin,*[,§] and Andrei V. Shevelkov*[,†]

[†]Department of Chemistry, Lomonosov Moscow State University, Moscow, Russia
[‡]National University of Forestry and Wood Technology of Ukraine, Lviv, Ukraine
[§]Max-Planck-Institut für Chemische Physik fester Stoffe, Dresden, Germany
[∥]EMAT, University of Antwerp, Antwerp, Belgium
[⊥]National Institute of Chemical Physics and Biophysics, Tallinn, Estonia
[#]European Synchrotron Radiation Facility, Grenoble, France

Ⓢ *Supporting Information*

ABSTRACT: Two new ternary arsenides, namely, $Eu_7Cu_{44}As_{23}$ and $Sr_7Cu_{44}As_{23}$, were synthesized from elements at 800 °C. Their crystal structure represents a new filled version of the $BaHg_{11}$ motif with cubic voids alternately occupied by Eu(Sr) and As atoms, resulting in a 2 × 2 × 2 superstructure of the aristotype: space group $Fm\bar{3}m$, a = 16.6707(2) Å and 16.7467(2) Å, respectively. The Eu derivative exhibits ferromagnetic ordering below 17.5 K. In agreement with band structure calculations both compounds are metals, exhibiting relatively low thermopower, but high electrical and low thermal conductivity.

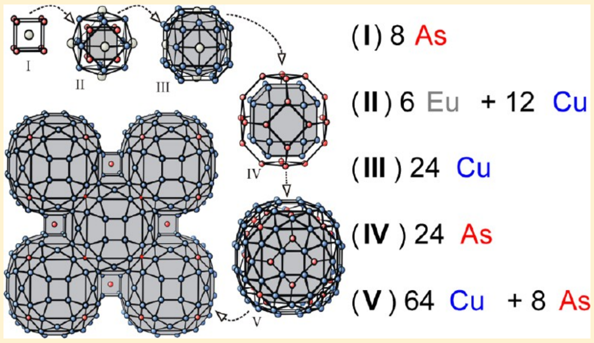

■ INTRODUCTION

Intermetallic clathrates—binary silicides of alkali metals—are analogs of gas hydrates and have been known since 1965,[1] but their chemistry and physics attracted significant attention of the scientific community since the late nineties due to their prospective applications as mid- and high-temperature thermoelectric materials.[2−7] The frameworks are mainly based on Si, Ge, and Sn. Their cavities are usually occupied by electropositive elements such as Eu, Ba, K, or Na, but in rare cases electronegative guest atoms such as Br, I, or Te were also observed.[8] It is shown that clathrates exhibit rather high thermoelectric figures of merit owing to a structural separation of moieties responsible for the efficient transport of charge carriers and for impeding the phonon transport.[7] This brings about a possibility of optimizing these properties almost independently. Recently, the family of clathrates has been expanded by compounds showing peculiar superstructures of various clathrate structure types and also by clathrate-like compounds.[9−16] Importantly, some of these compounds do not contain any group 14 element, for example, $Ba_8Au_{16}P_{30}$[14] and $Eu_2Ba_6Cu_{16}P_{30}$.[16] Although deviating from proper clathrates by composition and crystal structure, these compounds display properties that make them good candidates for creating new thermoelectric materials. In particular, $Ba_8Au_{16}P_{30}$ shows an exceptionally low thermal conductivity of 0.18 W m^{-1} K^{-1} at ambient temperature.[14] Motivated by this, we have undertaken a search for new clathrate-like compounds among complex pnictides of copper and silver.

The systems alkaline earth (A)−coinage metal (T)−pnictogen (Pn) host many attractive and peculiar ternary compounds. An incomplete list includes the clathrate and clathrate-like compounds $Ba_8Cu_{16}P_{30}$[15] and $Ba_2Cu_{18-x}As_{10}$,[17] a large family of $BaAl_4$-derived compounds AT_2Pn_2,[18−20] which are closely related to FeAs-based superconductors, and $BaCu_6Pn_2$ (Pn = P, As) containing Cu in an oxidation state smaller than +1.[21] In heavier pnictides and commonly also in phosphides, europium adopts the oxidation state +2 and behaves as a structural and electronic analog of alkaline earth metals, forming isostructural compounds. The semifilled 4f level of Eu^{2+} gives rise to pronounced, sometimes outstanding, magnetic phenomena. For instance, our recent studies in the A−Cu−P systems revealed two new compounds $A_2Cu_6P_5$ (A = Sr, Eu) along with a yet unique phase $EuCu_4P_3$, which exhibits three consecutive magnetic transitions below 50 K.[22] A crystal chemical peculiarity of these systems is that most structure

Received: July 22, 2014
Published: September 29, 2014

dx.doi.org/10.1021/ic5017615 | *Inorg. Chem.* 2014, 53, 11173−11184

Table 1. Crystallographic Data and Experimental Details for $Eu_{7-x}Sr_xCu_{44}As_{23}$ (x = 0, 1.26, 7) at 295 K (space group $Fm\bar{3}m$ (No. 225), Pearson symbol $cF296$, Z = 4)

composition	$Eu_7Cu_{44}As_{23}$ (x = 0)	$Eu_{5.74}Sr_{1.26}Cu_{44}As_{23}$ (x = 1.26)
unit cell parameters		
a (Å)[a]	16.6707(2)	16.6767(5)
V (Å^3)[a]	4633.0(2)	4638.0(4)
crystal size (mm^3)	0.010 × 0.025 × 0.035	0.015 × 0.040 × 0.080
diffractometer	Rigaku R-AXIS SPIDER	Rigaku AFC7
detector	image plate	
Weissenberg geometry	Saturn724+ CCD	
radiation, λ (Å)	(Ag Kα), 0.560 87	(Mo Kα), 0.710 73
scans, step (deg)	ω, 1.0	φ, 0.6
no. images	120	600
$2\theta_{max}$ (deg)	57.8	64.98
ranges in hkl	$-17 \leq h \leq 28$	$-25 \leq h \leq 24$
	$-28 \leq k \leq 21$	$-24 \leq k \leq 24$
	$-27 \leq l \leq 22$	$-24 \leq l \leq 22$
N (collected)	11 486	11 099
N (unique)	686	473
N observed [$I \geq 2\sigma(I)$]	628	437
R_{int}	0.024	0.042
refined parameters	28	30
$R1$ [$I \geq 2\sigma(I)$]	0.013	0.039
$wR2$ [$I \geq 2\sigma(I)$]	0.024	0.074
extinction coefficient	0.000 054(3)	0.000 008(1)
residual peaks (e$^-$·Å^{-3})	1.06/−0.74	0.88/−0.64
composition	$Sr_7Cu_{44}As_{23}$ (x = 7)	
unit cell parameters		
a (Å)[a]	16.7467(2)	
V (Å^3)[a]	4696.64(12)	
beamline	ID 31, ESRF	
detector	nine-crystal multianalyzer	
radiation, λ (Å)	synchrotron, 0.39996(1)	
2θ max	40°	
step size (deg 2θ)	0.002	
R_I/R_P	0.038/0.088	

[a] From X-ray powder diffraction data.

types are particularly sensitive to the nature of A, T, and Pn, and attempts to prepare isostructural compounds often lead to quite different results. For instance, analogues of $BaCu_6P_2$ or $BaCu_6As_2$ structures with Sr, Sb, or Ag do not exist.[21] Similarly, no compounds with the $A_2Cu_6P_5$ (A = Ca, Sr, Eu) structure were found among arsenides.[22]

A new compound $Eu_7Cu_{44}As_{23}$[23] was obtained during initial attempts to synthesize Eu-based arsenide with the $Ba_2Cu_{18-x}As_{10}$[17] structure. In line with aforementioned findings, we succeeded in preparing an isostructural phase, $Sr_7Cu_{44}As_{23}$. In the present paper, we report synthesis, crystal and electronic structure as well as magnetic and transport properties of these new compounds.

EXPERIMENTAL SECTION

Synthesis and Characterization. The starting materials for preparing $Eu_{7-x}Sr_xCu_{44}As_{23}$ (x = 1, 3.5, 5, 7) samples were ingots of Eu, Sr, and Cu and As powder (purity above 99%). All manipulations were carried out in an argon-filled glovebox (MBRAUN 120B-G, $p(O_2/H_2O) < 1$ ppm). The preparation technique was essentially the same as in the synthesis of the $A_2Cu_6P_5$ compounds.[11] In a typical run, a stoichiometric mixture of the elements (ca. 3% excess of electropositive metal was used to compensate for its volatility) were enclosed into carbon-lined evacuated quartz tubes. The samples were heated to 800 °C at ~30 °C/h, but with three 12 h plateaus at 200, 400, and 600 °C, and sintered at the final temperature for 48 h. The annealed mixtures were reground, pressed into pellets, and reannealed at 800 °C once or twice until equilibrium was attained. Single crystals of $Eu_7Cu_{44}As_{23}$ were obtained from a sample additionally arc-melted in purified argon, further annealed at 800 °C for two weeks, and subsequently quenched in cold water.

The phase analysis of the annealed samples was performed by using X-ray powder diffraction patterns recorded with a BRUKER D8 Advance diffractometer in reflection geometry using a LynxEye silicon strip detector, or with a Huber Imaging Plate Guinier Camera G670 (both Cu Kα_1 radiation, Ge (111) monochromator, λ = 1.540 598 Å).

For metallographic microstructure investigation the samples were embedded in a two-component epoxy resin with silver filler (H20E; EPO-TEK), which ensures discharge for electron-microscopic investigation. Areas of approximately 3 × 3 mm^2 were prepared by polishing, using a 0.25 μm diamond powder for finishing. Lubricants based on isopropanol/ethanol mixtures, which are dedicated for microstructure preparation of water-sensitive intermetallic phases, were used. Energy-dispersive X-ray spectroscopy (EDXS) was performed to determine chemical composition and to check for possible contamination by elements like oxygen. Wavelength-dispersive X-ray spectroscopy analysis (WDXS) was realized by employing a CAMECA SX100 Electron Microprobe with a tungsten cathode.

Crystal Structure Determination. The crystal structure of $Eu_7Cu_{44}As_{23}$ was determined from single-crystal X-ray diffraction data collected on a Rigaku R-AXIS SPIDER system consisting of curved image plate detector in Weissenberg geometry, equipped with a rotating anode source (Ag Kα) and Osmic VariMax X-ray optics. The atomic pattern of isotypic $Eu_{7-x}Sr_xCu_{44}As_{23}$ (x = 1.26(1)) was refined on data measured by Rigaku AFC7 diffraction system equipped with a Saturn724+ CCD detector (Mo Kα radiation). The single-crystal specimen was extracted from the sample with x = 1. Crystal structure solution and refinement were performed with the SHELX programs.[24] For the calculation of interatomic distances, the lattice parameters obtained from X-ray powder diffraction data were used (rutile TiO_2 as internal standard,[25] WinCSD software package[26]). Details on data collection and the crystal structure refinement are summarized in Table 1.

Attempts to obtain single crystals of $Sr_7Cu_{44}As_{23}$ failed; therefore, high-resolution powder X-ray diffraction (XRD) data were used for the crystal structure refinement. The diffraction pattern was collected at ambient temperature at beamline ID31 of the European Synchrotron Radiation Facility (ESRF) (λ = 0.399 96(1) Å, $2\theta_{max}$ = 40°) on a powdered sample enclosed in a quartz capillary with an outer diameter of 0.5 mm. Signals were measured by eight scintillation detectors, each preceded by a Si(111) analyzer crystal. For Rietveld refinements the WinCSD software[26] was used with starting values from the crystal structure of $Eu_7Cu_{44}As_{23}$. The refinement converged to low residuals and enabled the derivation of the atomic positions as well as anisotropic displacement parameters for all atoms.

$Eu_7Cu_{44}As_{23}$ was investigated using electron diffraction (ED) and high-resolution high-angle annular dark-field scanning transmission electron microscopy (HAADF-STEM). The ED patterns were recorded on an FEI Tecnai G2 electron microscope operated at 200 kV. The HAADF-STEM images were collected on a probe aberration-corrected microscope FEI Titan 50−80 operated at 300 kV. Simulated images were generated using the available structural model in QSTEM 2.22 software.

Band Structure Calculation. The electronic structures of $Eu_7Cu_{44}As_{23}$ and $Sr_7Cu_{44}As_{23}$ were calculated within the local-density approximation (LDA) of density-functional theory (DFT) using the full-potential FPLO code (version 9.05−39).[27] The 4f states of Eu atoms were treated as core states to focus on the properties of other valence electrons. In the scalar relativistic calculation, the exchange-correlation potential by Perdew and Wang[28] was used. Integrations in k space were performed by an improved tetrahedron method[29] on a grid of 12 × 12 × 12 k points evenly spread in the first Brillouin zone.

Physical Properties Measurement. The magnetization of polycrystalline sample pieces was measured with a MPMS SQUID (Quantum Design) and the VSM setup of a Physical Property Measurement System (PPMS, Quantum Design) in external magnetic fields between 0 and 5 T (SQUID) or 0 and 14 T (VSM) in the temperature range of 2−400 K. The heat capacity measurements were performed with a relaxation-type calorimeter (PPMS, Quantum Design) in magnetic fields of 0 and 7 T in the temperature range between 1.8 and 50 K. These measurements were done on small pellets with the sample weights of 20.9(1) and 8.1(1) mg for A = Eu and Sr, respectively. Low-temperature thermoelectric properties were measured using four-probe method with the TTO setup of a PPMS (Quantum Design) in the temperature range of 4−300 K in zero magnetic field. Thermal and electrical contacts (gold-plated Pb stripes) were fixed on rectangular-shaped pellets with a typical size of 8 × 3 × 2 mm^3 using silver-containing epoxy resin (Epotek H20E) hardened at 100 °C. Pellets were cold-pressed from powder samples at an external pressure of 100 bar. Densities of the obtained pellets were estimated geometrically 79−83% of the theoretical values.

■ RESULTS AND DISCUSSION

Synthesis. $Eu_7Cu_{44}As_{23}$ and $Sr_7Cu_{44}As_{23}$ were obtained as pure phases according to X-ray powder diffraction patterns (Figure 1). Most reflections of the diffraction patterns are indexed based on primitive cubic unit cells (e.g., a = 8.335 Å for Eu phase), which is characteristic for the $BaHg_{11}$ structure type. Weak additional reflections indicate doubling of the unit cell leading to the F-centered 8-fold superstructure.

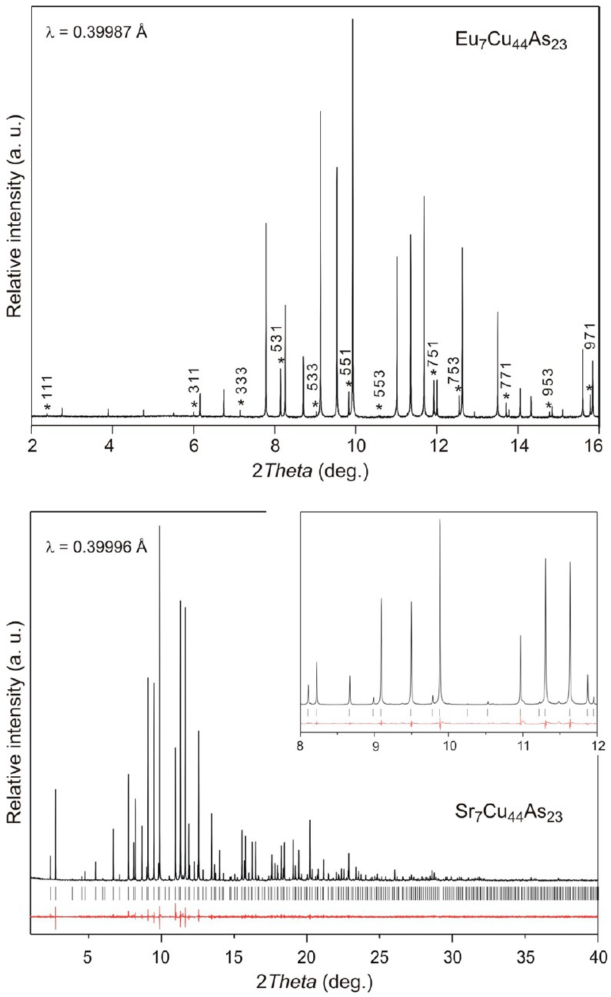

Figure 1. (upper) Powder X-ray diffraction pattern of $Eu_7Cu_{44}As_{23}$ and indices of peaks that reveal the doubling of a *P-subcell* due to the 2 × 2 × 2 superstructure, $a(Eu_7Cu_{44}As_{23}) \approx 2a(BaHg_{11})$. (lower) Graphical representation of the Rietveld refinement of $Sr_7Cu_{44}As_{23}$. Black line: experimental synchrotron XRD pattern; black ticks: peak positions; red line: the difference plot of calculated and experimental patterns.

Upon substituting Sr for Eu, the continuous solid solution $Eu_{7-x}Sr_xCu_{44}As_{23}$ (x = 0−7) is formed. The lattice parameter of the solid solution increases linearly with increasing the strontium content and agrees well with Vegard's rule: a = 16.6707(2) Å (x = 0), a = 16.6767(5) Å (x = 1.26), a = 16.7041(2) Å (x = 3.5), a = 16.7175(2) Å (x = 5), 16.7467(2) Å (x = 7).

Crystal Structure Solution and Refinement. Analysis of the data collected from an irregularly shaped single crystal extracted from the sample with nominal composition $Eu_{10}Cu_{60}As_{30}$ clearly indicated an F-centered cubic unit cell. The crystal structure was solved by the Patterson method, which provided positions of the Eu atoms. All other atomic sites were located from Fourier difference maps. In spite of very close atomic numbers for Cu and As (29 and 33, respectively), the distribution of these species on the atomic sites in the structure of $Eu_7Cu_{44}As_{23}$ could be clearly determined. To check the correctness of the distribution of Cu versus As atoms, we refined the occupancies of all Cu and As positions. This resulted in occupancies between 0.994(2) and 1.007(6) indicating full occupation of all Cu and As positions. In the

Table 2. Atomic Coordinates and Displacement Parameters for the Crystal Structures of $Eu_{7-x}Sr_xCu_{44}As_{23}$ (x = 0, 1.26, 7)

atom	site	x	y	z	U_{eq} (Å^2)
			$Eu_7Cu_{44}As_{23}$ (x = 0)		
Eu1	24*e*	0.24512(1)	0	0	0.00962(4)
Eu2	4*a*	0	0	0	0.01031(9)
Cu1	96*k*	0.13651(1)	x	0.25401(2)	0.01355(6)
Cu2	48*h*	0	0.18179(2)	y	0.01204(7)
Cu3	32*f*	0.41236(2)	x	x	0.01601(9)
As1	48*i*	1/2	0.17181(1)	y	0.00870(5)
As2	32*f*	0.10964(1)	x	x	0.00827(6)
As3	8*c*	1/4	1/4	1/4	0.0081(1)
As4	4*b*	1/2	1/2	1/2	0.0180(2)
			$Eu_{7-x}Sr_xCu_{44}As_{23}$ (x = 1.26)		
*A*1[a]	24*e*	0.24516(2)	0	0	0.01015(6)
*A*2[b]	4*a*	0	0	0	0.00978(8)
Cu1	96*k*	0.13654(1)	x	0.25395(2)	0.01531(7)
Cu2	48*h*	0	0.18179(2)	y	0.01359(10)
Cu3	32*f*	0.41241(2)	x	x	0.01836(7)
As1	48*i*	1/2	0.17190(1)	y	0.01030(8)
As2	32*f*	0.10981(2)	x	x	0.01007(5)
As3	8*c*	1/4	1/4	1/4	0.00841(9)
As4	4*b*	1/2	1/2	1/2	0.0182(2)
			$Sr_7Cu_{44}As_{23}$ (x = 7)		
Sr1	24*e*	0.24363(7)	0	0	0.0092(3)
Sr2	4*a*	0	0	0	0.0088(3)
Cu1	96*k*	0.13691(3)	x	0.25446(6)	0.0157(2)
Cu2	48*h*	0	0.18214(5)	y	0.0143(3)
Cu3	32*f*	0.41209(5)	x	x	0.0183(2)
As1	48*i*	1/2	0.17190(4)	y	0.0100(3)
As2	32*f*	0.11086(4)	x	x	0.0085(1)
As3	8*c*	1/4	1/4	1/4	0.0090(3)
As4	4*b*	1/2	1/2	1/2	0.0173(5)

[a] *A*1 = 0.839(2) Eu + 0.161 Sr. [b] *A*2 = 0.711(3) Eu + 0.289 Sr.

final steps of the structure refinement, all occupancies of the atomic sites were fixed to the ideal values. Subsequently, the structure model of $Eu_7Cu_{44}As_{23}$ was refined with anisotropic displacement parameters for all atoms. The composition resulting from the crystal structure determination ($Eu_7Cu_{44}As_{23}$) agrees well with that obtained by microprobe analysis ($Eu_{7.11(5)}Cu_{43.91(8)}As_{22.98(5)}$).

The crystal structure of the substituted compound $Eu_{7-x}Sr_xCu_{44}As_{23}$ was also determined from single-crystal data using atomic parameters of $Eu_7Cu_{44}As_{23}$ as starting values. The atomic distribution of Eu and Sr at the 24*e* and 4*a* positions was refined, which resulted in the Eu/Sr ratio of 5.74(1):1.26(1). The obtained composition $Eu_{7-x}Sr_xCu_{44}As_{23}$ (x = 1.26) agrees very well with the results of the microprobe analysis ($Eu_{5.68(4)}Sr_{1.3(1)}Cu_{43.95(5)}As_{22.99(4)}$) and deviates slightly from the nominal composition of the sample ($Eu_6Sr_1Cu_{44}As_{23}$) from where the single-crystal specimen was taken.

The results of $Sr_7Cu_{44}As_{23}$ XRPD pattern fitting are presented in Figure 1. High quality of the diffraction pattern, collected up to sin θ/λ of 0.85, allowed us to refine anisotropic displacement parameters for all atomic positions in the structure of $Sr_7Cu_{44}As_{23}$. The final atomic parameters and selected interatomic distances are collected in Tables 2 and 3, respectively; a view of the crystal structure is given in Figure 2 (upper).

Transmission Electron Microscopy Study. Typical ED patterns taken along the main crystallographic directions [100], [110], and [111] in the $Eu_7Cu_{44}As_{23}$ crystal structure are represented in Figure 2 (lower). They are consistently indexed on an *F*-centered cubic lattice with cell parameter around 16 Å. The ED observations are fully consistent with the crystallographic data provided on the basis of X-ray diffraction.

HAADF-STEM images collected along the [100] and [110] directions are shown in Figure 3. In this microscopy technique, the intensity of a projected column scales approximately as $I \approx Z^2$, where Z is averaged atomic number along the column. Therefore, the HAADF-STEM images provide information on the distribution of atomic species in the structure. Since the structure of $Eu_7Cu_{44}As_{23}$ is rather complex, the interpretation of the HAADF-STEM data is not straightforward. It requires calculation of theoretical HAADF-STEM images and their comparison with experimental ones. The [100] and [110] HAADF-STEM images calculated using the structure data from Table 2 are in perfect agreement with the experimentally observed contrast, confirming the correctness of the structure model. Note that no extended defects were observed in this material.

Description of the Crystal Structure. The atomic arrangement in $Eu_7Cu_{44}As_{23}$ (Figure 2) reproduces main features of the $BaHg_{11}$ structure.[30] The Eu1 atoms are located at the Ba positions, whereas Cu and As occupy the Hg sites in an ordered manner. Additionally, cubic voids at the origin of the $BaHg_{11}$ structure are filled alternatingly by europium (Eu2) or arsenic (As4) atoms, causing a doubling of the unit cell, $a(Eu_7Cu_{44}As_{23}) \approx 2a(BaHg_{11})$, and thus leading to a 2 × 2 × 2 superstructure.

Table 3. Selected Interatomic Distances in $Eu_{7-x}Sr_xCu_{44}As_{23}$ (x = 0, 1.26, 7)

bond		distance (Å)		
		(x = 0)	(x = 1.26)	(x = 7)
$A1^a$	−4As1	3.1814(1)	3.1830(3)	3.2076(8)
	−4Cu2	3.2092(2)	3.2105(3)	3.2193(9)
	−4Cu1	3.2217(3)	3.2235(2)	3.2474(5)
	−4As2	3.4326(2)	3.4353(3)	3.4404(9)
	−4Cu3	3.4702(2)	3.4709(4)	3.506(1)
	−1A2	4.0863(2)	4.0884(3)	4.080(1)
A2	−8As2	3.1659(3)	3.1717(3)	3.2154(6)
	−6A1	4.0863(2)	4.0884(3)	4.080(1)
Cu1	−1As2	2.4887(4)	2.4852(4)	2.483(1)
	−2Cu1	2.5811(5)	2.5828(4)	2.573(1)
	−2As1	2.6560(2)	2.6574(3)	2.6685(7)
	−1As3	2.6765(3)	2.6767(2)	2.6795(5)
	−2Cu2	2.6830(2)	2.6837(3)	2.7013(7)
	−2Cu1	2.7703(5)	2.7690(4)	2.784(1)
	−1Cu3	2.8802(5)	2.8837(4)	2.884(1)
	−1A1	3.2217(3)	3.2235(2)	3.2474(5)
Cu2	−2As1	2.4462(3)	2.4456(4)	2.450(1)
	−2As2	2.4968(3)	2.4970(3)	2.5093(8)
	−4Cu1	2.6830(2)	2.6837(3)	2.7013(7)
	−2A1	3.2092(2)	3.2105(3)	3.214(1)
Cu3	−3As1	2.4643(3)	2.4672(4)	2.475(1)
	−1As4	2.5305(5)	2.5302(3)	2.5500(8)
	−3Cu1	2.8802(5)	2.8837(4)	2.884(1)
	−3Cu3	2.9220(6)	2.9216(5)	2.944(1)
	−3A1	3.4702(2)	3.4709(4)	3.506(1)
As1	−2Cu2	2.4462(3)	2.4456(4)	2.450(1)
	−2Cu3	2.4643(3)	2.4672(4)	2.475(1)
	−4Cu1	2.6560(2)	2.6574(3)	2.6685(7)
	−2A1	3.1814(1)	3.1830(3)	3.2076(8)
As2	−3Cu1	2.4887(4)	2.4852(4)	2.483(1)
	−3Cu2	2.4968(3)	2.4970(3)	2.5093(8)
	−1A2	3.1659(3)	3.1717(3)	3.2154(6)
	−3A1	3.4329(2)	3.4353(3)	3.4404(9)
As3	−12Cu1	2.6725(3)	2.6767(2)	2.6795(5)
As4	−8Cu3	2.5305(5)	2.5302(3)	2.5500(8)
	−6A1	4.2496(3)	4.2499(3)	4.293(1)

[a] A = Eu or Sr.

Coordination polyhedra in $Eu_7Cu_{44}As_{23}$ are similar to those observed in the structure of the aristotype $BaHg_{11}$ (Figure 4). Each copper species is tetrahedrally coordinated by As atoms. The Cu2[As]$_4$ and Cu3[As]$_4$ tetrahedra are slightly distorted with d(Cu2−As) = 2.45−2.50 Å and d(Cu3−As) = 2.46−2.53 Å. The Cu1[As]$_4$ tetrahedron is less regular with one short Cu−As contact of 2.48 Å and three elongated distances of 2.65−2.68 Å. The significant deviation from the ideal tetrahedron is eventually caused by two Cu1−Cu1 contacts at 2.58 Å, which are significantly shorter than other Cu−Cu distances in the structure (2.68−2.92 Å). The coordination spheres of copper atoms are completed by Cu and Eu species, increasing their coordination numbers to 12, 10, 13 for Cu1, Cu2, and Cu3, respectively.

The coordination of As atoms is different among four occupied crystallographic positions. The As3 atoms are surrounded cuboctahedrally by 12 Cu atoms. The environments of the As1 and As2 positions are less regular and contain 10 atoms: eight Cu and two Eu for As1, and six Cu and four Eu for As2. No As−As contacts are observed in $Eu_7Cu_{44}As_{23}$ as expected for ternary arsenides with the arsenic content less than 33 atom %.

The Eu1 atom is located in the center of a tetragonal hexagonprism (eight Cu + eight As). Its coordination is completed up to CN = 20 by four Cu atoms each capping a hexagonal face. The tetragonal faces of six adjacent Eu1-[$Cu_{12}As_8$] polyhedra form cubic voids occupied alternatingly by the Eu2 and As4 atoms. In the $BaHg_{11}$ structure these voids remain empty. As a consequence, Eu2 and As4 atoms both have a similar coordination environment (CN = 8 + 6) consisting of eight smaller As or Cu atoms and six larger Eu atoms located at the apexes of an almost perfect cube or octahedron, respectively. Such cubic environment for As atoms is unique for ternary arsenides with metal-to-nonmetal ratio of 2:1. Nevertheless, due to the different size of the central atoms (Eu or As) the resulting polyhedra are of slightly different shape. In the case of the As4 atom, smaller Cu atoms are centering each triangular face of the Eu_6 octahedron. The polyhedron around Eu2 is more convex as each triangular face is capped by one As atom. The latter arrangement very much resembles a CsCl-like motif. Note that the ordering of the copper and arsenic atoms over the framework positions of the parent $BaHg_{11}$ structure causes the difference in the volume of cubes and facilitates the ordering of As and Eu that leads to the superstructure formation.

While Ba atoms in $BaHg_{11}$ are isolated by the mercury species, the Eu atoms in the structure of $Eu_7Cu_{44}As_{23}$ are grouped into Eu[Eu_6] octahedral units (Figure 5, upper left) due to incorporation of additional Eu atoms in the cubic cavities of the [CuAs] framework. These Eu2[Eu1]$_6$ units are surrounded by Cu and As in such a way that Eu_7[$Cu_{60}As_{32}$] clusters are formed, and these clusters may be regarded as six condensed coordination polyhedra Eu1[$Cu_{8+4/2}As_{4+4/3}$] around Eu2 atoms (Figure 5, lower). They are further separated by the As4[Cu_8] cubes and the As3[Cu_{12}] cubooctahedra, but are condensed via triangular faces forming a 3D framework (Figure 5, lower).

Alternatively the crystal structure of $Eu_7Cu_{44}As_{23}$ can be described as a set of shells (nested polyhedra) around the Eu2 position. As shown in Figure 6, the first shell is formed by eight As atoms (cube). The second shell is represented by a cuboctahedron with six additional Eu atoms opposite to the tetragonal faces of the cubes. The third, fourth, and fifth shells are formed by 24Cu, 24As, and 64Cu+8As atoms, respectively. These last shells are separated by As[Cu_8] cubes and partially interpenetrate each other in the areas where As[Cu_{12}] cuboctahedra are formed.

The group−subgroup relation between the aristotype $BaHg_{11}$ and $Eu_7Cu_{44}As_{23}$ with the respective reduction in translation symmetry, transformation of the unit cell, and coordinates as well as splitting of the corresponding Wyckoff positions are shown in Figure 7. The structural motif of $Eu_7Cu_{44}As_{23}$ is a first representative of an ordered and filled ternary derivative of the $BaHg_{11}$ structure type.[30] All respective crystal structures reported until now represent either binary compounds, for example, MHg_{11} (M = K, Rb, Ba, Sr)[31] or ternary phases with randomly occupied positions.[32,33] In quaternary $Y_3TaNi_{6.3}Al_{25.84}$ phase[34] an additional position at the centers of cubic voids is occupied corresponding to the Eu2 and As4 sites in $Eu_7Cu_{44}As_{23}$. While these positions are only partially and randomly occupied by Ni atoms (about 15%) in $Y_3TaNi_{6.3}Al_{25.84}$, the symmetry of the $BaHg_{11}$ substructure does not change due to intercalation of additional Ni atoms at

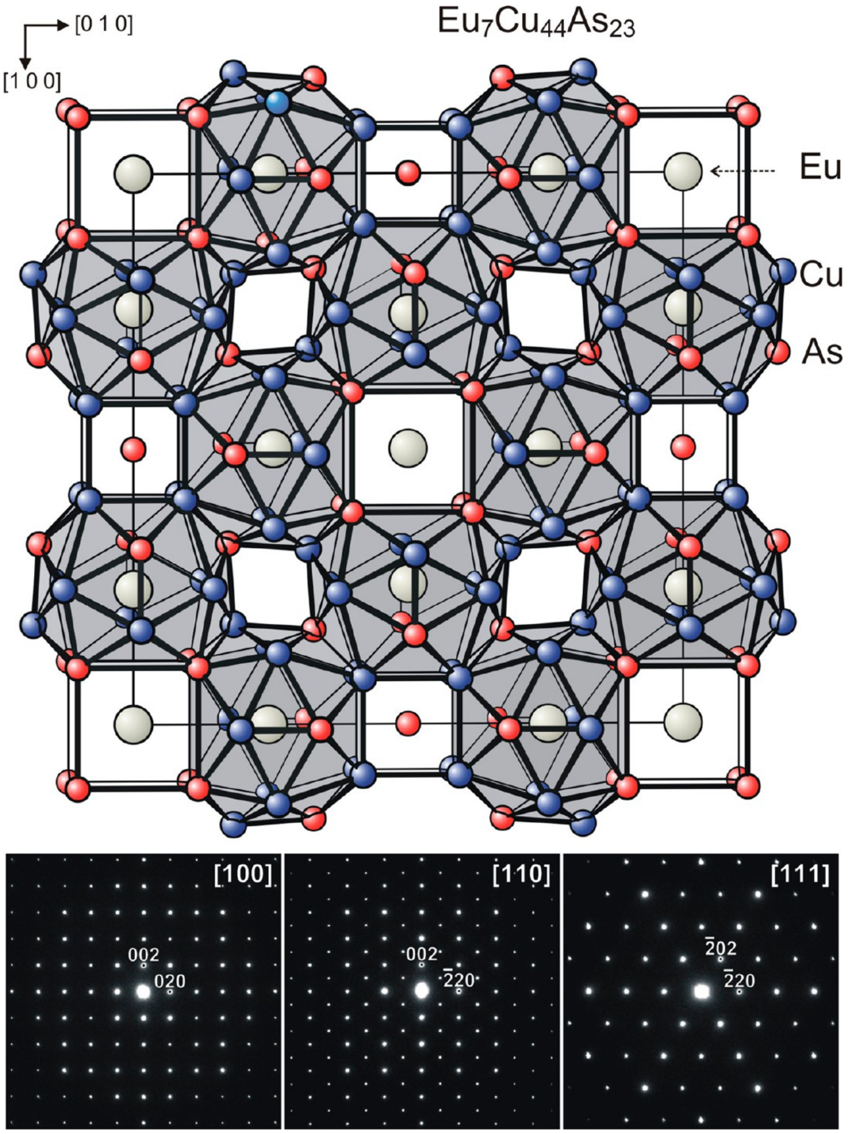

Figure 2. (upper) Projection of the crystal structure of $Eu_7Cu_{44}As_{23}$ along [001]. For visualization only part of the structure with $z = \pm\ 0.182$ is shown. (lower) ED patterns along the main crystallographic axes of the crystal structure of $Eu_7Cu_{44}As_{23}$.

the crystallographic 1*a* position (space group $Pm\bar{3}m$). The same structural features are observed in $Ca_3Au_{6.8}Al_{26}Ti$,[35] where the 1*a* atomic site is partially occupied (~0.8) by Au.

Recently four different derivatives of $BaHg_{11}$ were reported in the Ce–Pd–Ga system.[36] The rhombohedral, orthorhombic, and two cubic $CePd_{3-x}Ga_{8\pm y}$ gallides differ in their chemical composition and respective synthetic route. Among these gallides, the crystal structure of $CePd_{2.69}Ga_{8.31}$ is the most interesting for the present discussion owing to the unit cell parameters similar to those of $Eu_7Cu_{44}As_{23}$: the 2 × 2 × 2 superstructure of $BaHg_{11}$, space group $Fm\bar{3}m$, unit cell parameter a = 16.898 Å. A detailed comparison of both derivatives of $BaHg_{11}$ showed the following differences. Whereas the "empty" position in the original $BaHg_{11}$ substructure (1*a* in $Pm\bar{3}m$) remains unoccupied in $CePd_{2.69}Ga_{8.31}$, in the $Eu_7Cu_{44}As_{23}$ structure the respective position is occupied alternatingly by Eu and As atoms. The first coordination spheres around these sites are also different. In $Eu_7Cu_{44}As_{23}$ this position resides in a regular cube, while these cubes are deformed in $CePd_{2.69}Ga_{8.31}$. Thus, $m\bar{3}m$ point symmetry of this position in the $BaHg_{11}$ structure is retained in $Eu_7Cu_{44}As_{23}$ only, while in $CePd_{2.69}Ga_{8.31}$ this point symmetry is reduced to $4\bar{3}m$. Even though both structures are described in the same space group, symmetry reduction is different. As one consequence, the crystal structure of $Eu_7Cu_{44}As_{23}$ is described in the same setting as for $BaHg_{11}$, while for $CePd_{2.69}Ga_{8.31}$ the origin is shifted by 1/4 1/4 1/4. Additional information on the relationships of discussed compounds can be found in Figure 7.

$Eu_7Cu_{44}As_{23}$ and $Sr_7Cu_{44}As_{23}$ are isostructural because Eu^{2+} and Sr^{2+} possess only slightly different radii and thus may easily replace one another in various compounds including complex pnictides, $Eu_2Cu_6P_5$ and $Sr_2Cu_6P_5$ serving as representative examples.[22] Consequently, mixing Eu^{2+} and Sr^{2+} in $Eu_{7-x}Sr_xCu_{44}As_{23}$ (x = 1.26) does not lead to a segregation of strontium in any of the two positions for the *A* cation; Sr only slightly prefers the 4*a* site (Table 2). A slight increase in unit cell parameter is observed upon replacing Eu by Sr, reflecting larger atomic radius of Sr, which induces some elongation of the *A*–As distances to the Eu–As ones (Table 3). At the same time, the Cu–As and Cu–Cu contacts remain almost unchanged.

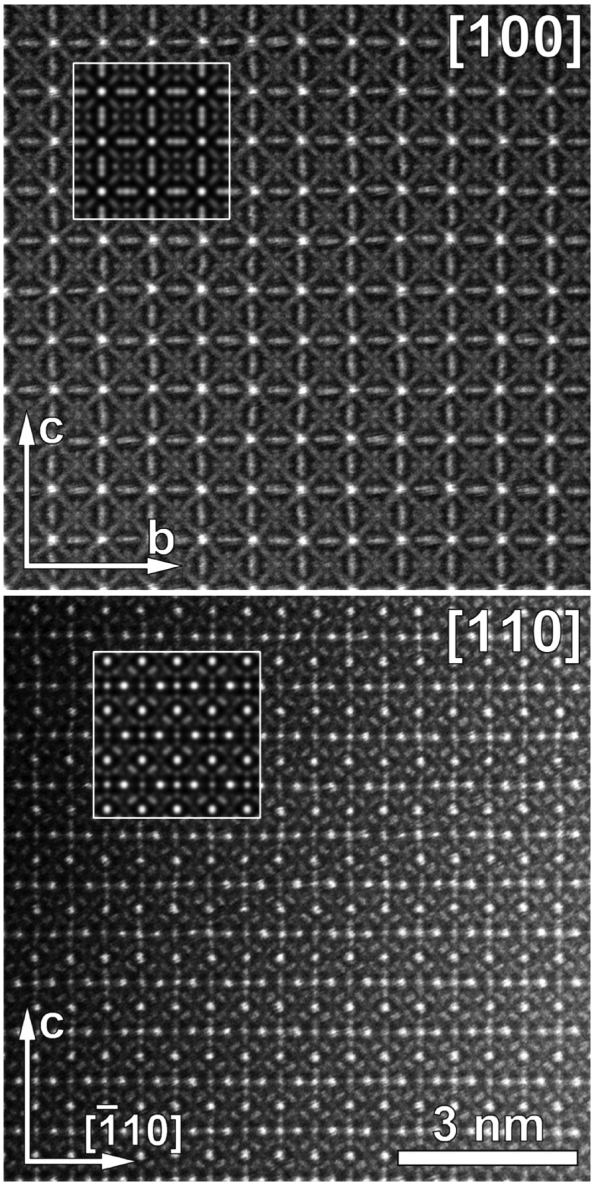

Figure 3. [100] and [110] HAADF-STEM images of $Eu_7Cu_{44}As_{23}$. (insets) The calculated images (thickness t = 10 nm).

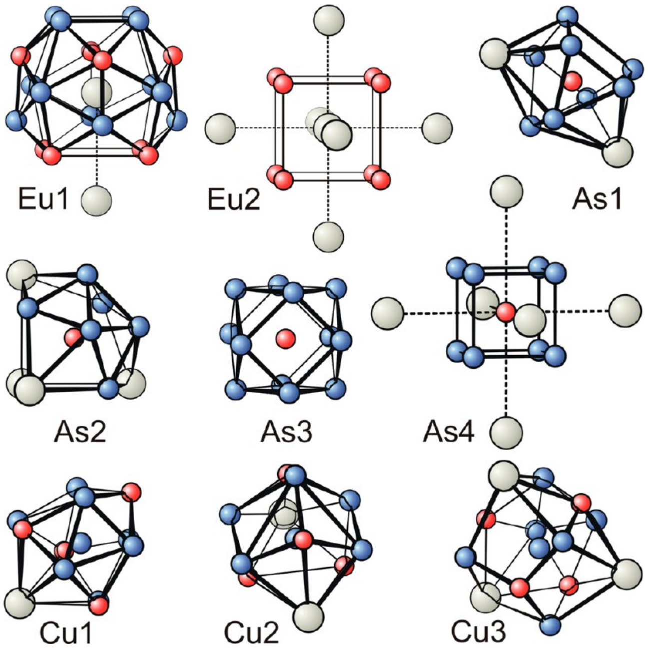

Figure 4. Coordination polyhedra in $Eu_7Cu_{44}As_{23}$.

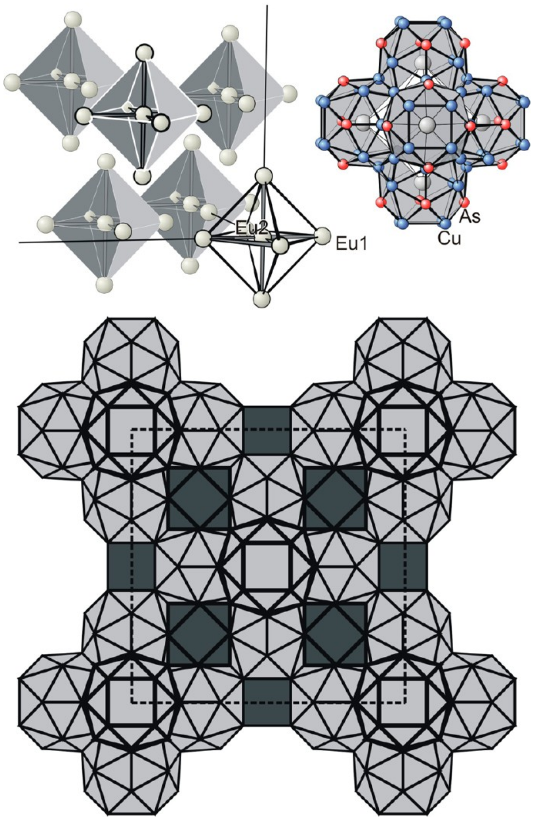

Figure 5. (upper) The Eu2[Eu1]$_6$ units forming a europium substructure in $Eu_7Cu_{44}As_{23}$ (upper left). $Eu_7[Cu_{60}As_{32}]$ cluster composed by condensed $Eu1[Cu_{8+4/2}As_{4+4/3}]$ polyhedra around Eu2 atoms. (lower) Stacking of the $Eu_7[Cu_{60}As_{32}]$ clusters involving $As[Cu_8]$ cubes and $As[Cu_{12}]$ cubooctahedra.

Electronic Structure. The calculated density of states (DOS) plots for $Eu_7Cu_{44}As_{23}$ and $Sr_7Cu_{44}As_{23}$ are presented in Figure 8. These isostructural compounds adopt similar electronic structures (Figure 8a). At low energies the band structures include two regions with bonding character. The first region located between −13 and −11 eV is due to the mixing of As 4s, Cu 4s, and Cu 4p orbitals, whereas the second one between −7 and −4 eV is composed of As 4p and Cu 3d states. The energy range between −4 and 1 eV is primarily representing Cu 3d states with an admixture of As 4p states for both compounds, and includes a small additional contribution from Eu 5d states in the case of $Eu_7Cu_{44}As_{23}$. Note that the 4*f* states of the Eu atoms are treated as core states and are therefore eliminated from the DOS plot. Thus, Cu 3d and As 4p states provide the major contributions to the density of states at the Fermi level for both arsenides, in the case of $Eu_7Cu_{44}As_{23}$, Eu 5d states also contribute to the DOS at $E = E_F$. In the energy region between 1 and 4 eV, the density of states is composed of As 4p, Cu 4s, and Cu 4p states with additional contribution from Sr 4d states in the case of $Sr_7Cu_{44}As_{23}$.

Analysis of the partial DOS reveals that there are several contributions to the bonding and nonbonding states in the

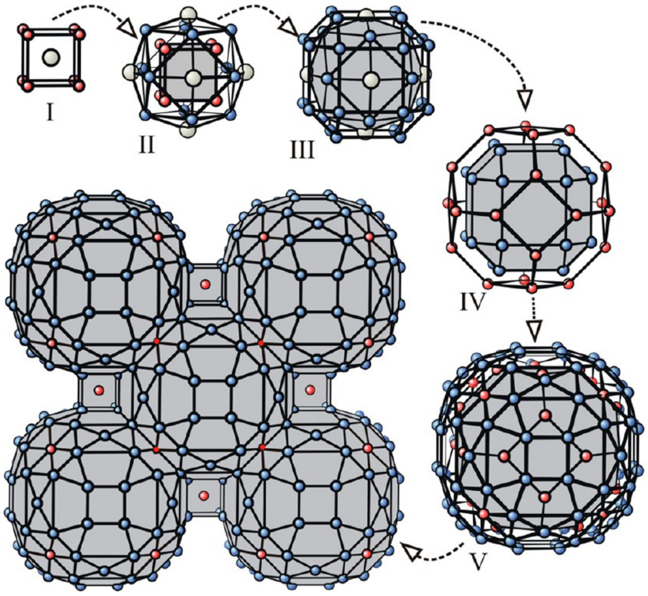

Figure 6. Endohedral clusters in $Eu_7Cu_{44}As_{23}$ regarded as a sequence of atomic shells surrounding the Eu2 atom at certain distances: (**I**), 3.16 Å (8As); (**II**) 4.08−4.28 Å (6Eu+12Cu); (**III**) 5.32 Å (24Cu); (**IV**), 6.17−6.28 Å (24As); (**V**) 7.17−7.66 Å (64Cu+8As). Europium, copper, and arsenic atoms are shown as gray, blue, and red circles, respectively.

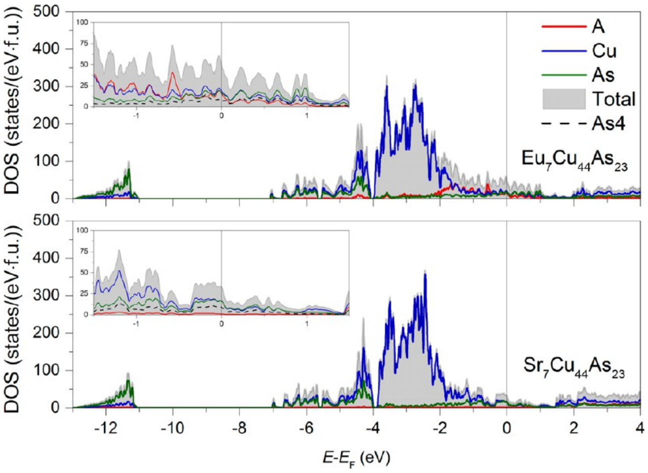

Figure 8. Calculated electronic density of states (DOS) for $Eu_7Cu_{44}As_{23}$ (upper) and $Sr_7Cu_{44}As_{23}$ (lower). The position of the Fermi level is indicated by the solid vertical line. (inset) DOS near the Fermi level; the As4 contribution is indicated by the dashed line.

energy region between −7 and 1 eV. All Cu atoms, namely Cu1, Cu2, and Cu3, contribute to the DOS significantly. On the other hand only As3 and As4 positions are involved in the formation of valence states. It is remarkable that As4, which is the only As atom accommodated in the voids of the parent $BaHg_{11}$ structure, provides about half of the total As contribution at the Fermi level (see the dashed line in the inset of Figure 8), even though there are only four atoms of this type per unit cell, as compared to 92 atoms of As in total. Therefore, the chemical and structural changes associated with the filling of voids in the $BaHg_{11}$ structure foster metallicity of the compound.

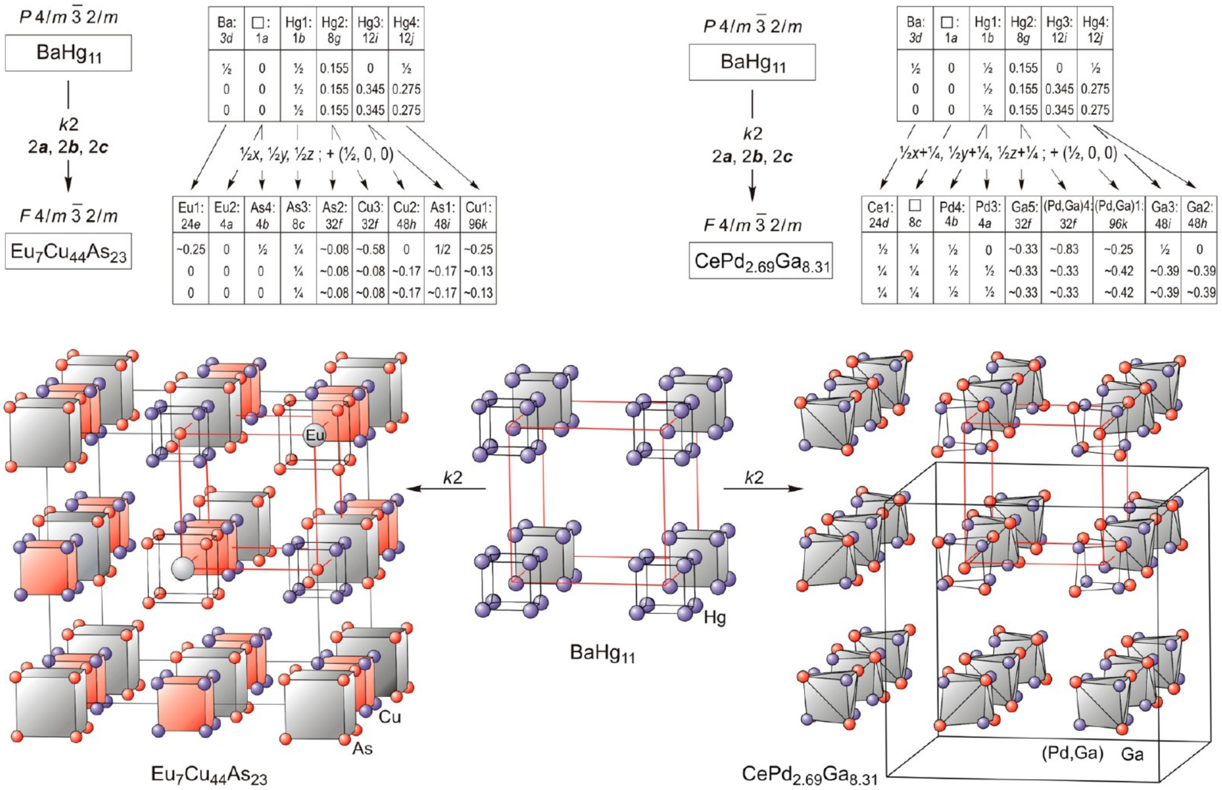

Ba: *3d*	□: 1*a*	Hg1: 1*b*	Hg2: 8*g*	Hg3: 12*i*	Hg4: 12*j*
½	0	½	0.155	0	½
0	0	½	0.155	0.345	0.275
0	0	½	0.155	0.345	0.275

Eu1: 24*e*	Eu2: 4*a*	As4: 4*b*	As3: 8*c*	As2: 32*f*	Cu3: 32*f*	Cu2: 48*h*	As1: 48*i*	Cu1: 96*k*
~0.25	0	½	¼	~0.08	~0.58	0	1/2	~0.25
0	0	0	¼	~0.08	~0.08	~0.17	~0.17	~0.13
0	0	0	¼	~0.08	~0.08	~0.17	~0.17	~0.13

Ba: *3d*	□: 1*a*	Hg1: 1*b*	Hg2: 8*g*	Hg3: 12*i*	Hg4: 12*j*
½	0	½	0.155	0	½
0	0	½	0.155	0.345	0.275
0	0	½	0.155	0.345	0.275

Ce1: 24*d*	□ 8*c*	Pd4: 4*b*	Pd3: 4*a*	Ga5: 32*f*	(Pd,Ga)4: 32*f*	(Pd,Ga)1: 96*k*	Ga3: 48*i*	Ga2: 48*h*
½	¼	½	0	~0.33	~0.83	~0.25	½	0
¼	¼	½	½	~0.33	~0.33	~0.42	~0.39	~0.39
¼	¼	½	½	~0.33	~0.33	~0.42	~0.39	~0.39

Figure 7. (upper) Graphical representation of the group−subgroup relations for $Eu_7Cu_{44}As_{23}$ and $CePd_{2.69}Ga_{8.31}$ with the parent structure of $BaHg_{11}$. (lower) The corresponding atomic positions in the crystal structures of $Eu_7Cu_{44}As_{23}$ (left) and $CePd_{2.69}Ga_{8.31}$ (right). The unit cell of $BaHg_{11}$ and the corresponding superstructures are shown as red and black cubes, respectively. For more details, see text.

The majority of Cu 3d states (more than 75% of the total DOS) are located below the Fermi level. Therefore, we can consider the $A_7Cu_{44}As_{23}$ arsenides as Cu^{1+}-based compounds. The hybridization between Cu^+ and As renders them metallic. Our calculations also show that the substitution of Eu by Sr has substantial effects on the electronic structure, as Eu 5d states increase the DOS at the Fermi level. Thus, the difference between the Sr and Eu arsenides lies in the contribution of the A atoms. In the case of Eu-based compound, both Eu1 and Eu2 positions make significant contribution to the DOS, while for the Sr-based compound the Sr1 and Sr2 atoms are not involved in the formation of bonding or nonbonding states.

In our calculations, we find $N(E_F)$ = 49.2 and 32.0 states/(eV·f.u.) for $Eu_7Cu_{44}As_{23}$ and $Sr_7Cu_{44}As_{23}$, respectively, which results in Sommerfeld coefficients of the electronic specific heat γ_{bare} = 0.116 and 0.076 J/(mole·K^2) and Pauli paramagnetic contributions to the susceptibility $\chi_{\text{Pcalc}} = 1.592 \times 10^{-3}$ and 1.036×10^{-3} emu/mol.

Magnetic Properties and Heat Capacity. To corroborate our microscopic picture of the electronic structure, we studied thermodynamic properties of both compounds in different applied magnetic fields. Figure 9 (upper) shows magnetic susceptibility versus T dependence for $Eu_7Cu_{44}As_{23}$. At low temperatures, a strong enhancement of the susceptibility indicates ferromagnetic ordering below ~20 K. The field-dependent magnetization of the sample at 2 K (shown in the inset of Figure 9, upper) confirms ferromagnetism of $Eu_7Cu_{44}As_{23}$. The magnetic moment rapidly increases with increasing magnetic field and saturates above H = 2 T with a saturation moment $M_S \approx 7\ \mu_B$ per Eu atom. At temperatures above 20 K the magnetic susceptibility of $Eu_7Cu_{44}As_{23}$ follows the Curie–Weiss law, as presented in Figure 9, lower. From the fit of the 5 T experimental data, we derive θ_{CW} = 17.02(8) K and μ_{eff} = 7.94(1) μ_B per Eu atom. Both M_S and μ_{eff} values indicate the Eu^{2+} state (4f^7) for Eu atoms, as in this state $J = S = 7/2$ and $L = 0$ yielding $M_S = gJ\mu_B = 7\ \mu_B$ per Eu atom (g = 2 for Eu^{2+} is the Landé g-factor) and $\mu_{\text{eff}} = g(S(S+1))^{1/2} = 7.94\ \mu_B$ per Eu atom.

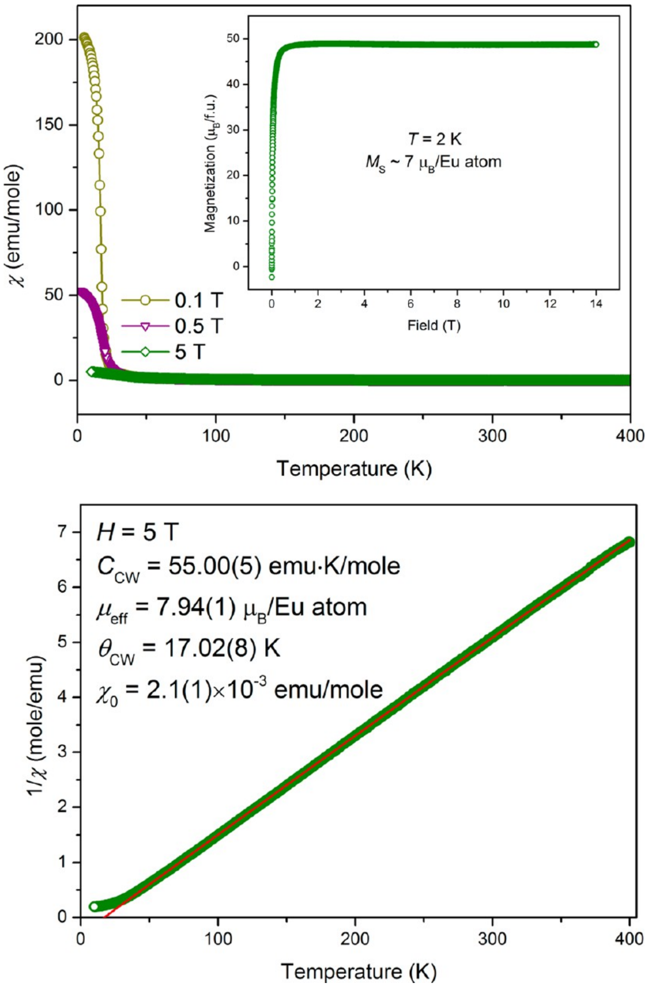

Figure 9. (upper) Temperature dependence of the magnetic susceptibility of $Eu_7Cu_{44}As_{23}$. (lower) (inset) The magnetization of the sample at 2 K vs magnetic field strength. $1/\chi$ vs T plot in 5 T magnetic field (○) and a modified Curie–Weiss law fit (solid line) of the experimental data.

The measurements of the $Eu_7Cu_{44}As_{23}$ heat capacity in a zero magnetic field (Figure 10) confirm the second-order phase transition for $Eu_7Cu_{44}As_{23}$ at $T_C \approx 17.3$ K. The magnetic nature of this transition is evidenced by the suppression of the anomaly in the applied magnetic field. At 0 T, the magnetic contribution to the heat capacity is partly released below T_C in the ferromagnetically ordered state, while in the applied field of 7 T the transition disappears, and the magnetic entropy shifts to higher temperatures. This results in larger values of the heat capacity in the zero field rather than in 7 T field below the Curie temperature T_C, and vice versa above T_C. It was shown[37] that the specific heat of the Eu^{2+}-based low-temperature ferromagnets, EuO and EuS, follows the predictions of the spin-wave theory below 4 K. According to this, we approximated the heat capacity of $Eu_7Cu_{44}As_{23}$ as $c_p = \gamma T + AT^{3/2} + BT^{5/2}$ in the temperature range between 1.8 and 4 K (inset, Figure 10). In this equation we neglected the lattice term CT,[3] which is expected to be much lower than the magnetic terms below 4 K. However, because of the small temperature range of the approximation, it is not possible to extract all three terms γ, A, and B from the experimental data, and for the final fit we used the fixed calculated value of γ_{bare} = 0.116 J/(mole·K^2). The fit results in A = 1.71(3) J/(mole·K$^{5/2}$) and B =

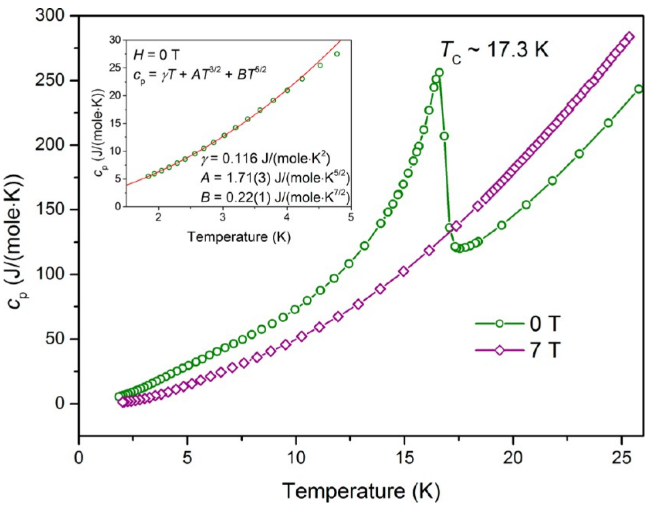

Figure 10. Heat capacity vs temperature plot in magnetic fields of 0 and 7 T for $Eu_7Cu_{44}As_{23}$. The experimental (○) values and the calculated (solid line) magnetic contribution to the heat capacity at low temperatures are presented in the inset.

0.22(1) J/(mole·K$^{7/2}$), which exceed the corresponding values for EuS A = 0.23 J/(mole·K$^{5/2}$) and B = 0.055 J/(mole·K$^{7/2}$) obtained for EuS,[38] because $Eu_7Cu_{44}As_{23}$ contains 7 magnetic ions per formula unit.

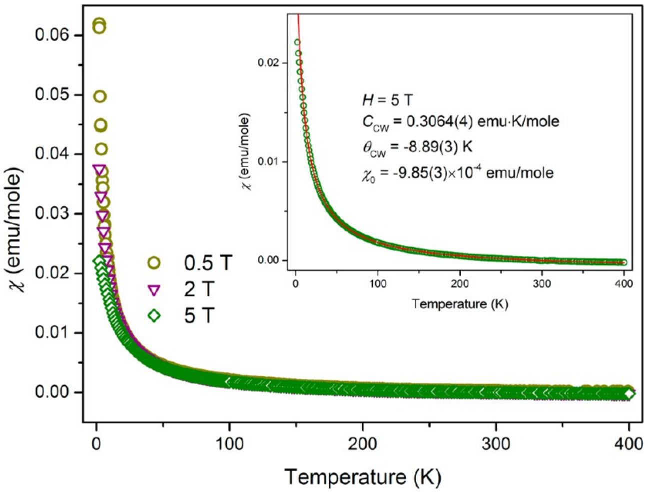

Figure 11. Temperature dependence of the magnetic susceptibility of $Sr_7Cu_{44}As_{23}$. (inset) A modified Curie−Weiss law fit (red solid line) of the experimental data in 5 T magnetic field.

The magnetic susceptibility of $Sr_7Cu_{44}As_{23}$ is shown in Figure 11. This compound displays an almost temperature-independent magnetic susceptibility between 150 and 400 K. An upturn of χ at low temperatures is most likely caused by paramagnetic impurities in the sample. We fitted the $\chi(T)$ data obtained in the 5 T field by a modified Curie−Weiss law $\chi = \chi_0 + (C_{CW}/(T + \theta_{CW}))$ and extracted the fitting parameters, which are presented in the inset of Figure 11. The C_{CW} value corresponds to ~0.03% of the $S = 1/2$ species.

The obtained value of χ_0 enables us to estimate Pauli paramagnetic contribution to the magnetic susceptibility of $Sr_7Cu_{44}As_{23}$. The χ_0 susceptibility can be written as $\chi_0 = \chi_{core} + \chi_L + \chi_{VV} + \chi_P$, where χ_{core} is the diamagnetic orbital contribution from the electrons (core diamagnetism), χ_L is the Landau orbital diamagnetism of the conduction electrons, χ_{VV} is the Van Vleck paramagnetic orbital contribution, and χ_P is the Pauli paramagnetic spin susceptibility of the conduction electrons. For $Sr_7Cu_{44}As_{23}$, the diamagnetic susceptibility χ_0 indicates quasi-free-electrons with $\chi_L = -(m/m^*)(2\chi_P/3)$ and $\chi_{VV} \approx 0$,[39] where m is the free electron mass and m^* is the effective mass of the charge carriers. Assuming $m^* = m$, the Pauli susceptibility can be written as $\chi_P = 3(\chi_0 - \chi_{core})$. To calculate χ_{core}, we used Pascal constants for Sr^{2+}, Cu^+, and As(V) species as given in ref 40. Note that the value for As, -43×10^{-6} emu/mol, represents covalent As species and resembles typical diamagnetic contributions of isoelectronic anions, such as Br^- (-34.6×10^{-6} emu/mol) and Se^{2-} (-48×10^{-6} emu/mol).

The resulting value of $\chi_P = 1.808 \times 10^{-3}$ emu/mol exceeds the calculated one, which is $\chi_{Pcalc} = 1.036 \times 10^{-3}$ emu/mol. This deviation can be attributed to an uncertainty in the estimation of the diamagnetic orbital contribution χ_{core} for the compound with mixed metallic and covalent type of bonding.

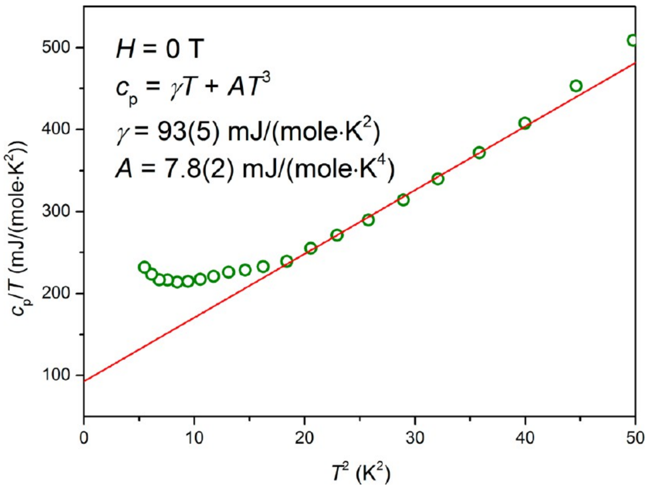

Figure 12. Specific heat c_p/T vs T^2 plot for $Sr_7Cu_{44}As_{23}$. The solid line presents a linear fit for the estimation of γ.

The specific heat c_p/T versus T^2 plot for $Sr_7Cu_{44}As_{23}$ is presented in Figure 12. Experimental data generally deviate from the simple linear behavior, which is expected according to $c_p = \gamma T + AT^3$, where the first term stands for the electronic contribution of a metal, and the second term is the low-temperature phonon contribution predicted by the Debye model. We tentatively assign this linear behavior to the T = 4.3−6.3 K temperature range. The deviations of the data from the linearity indicate the complexity of the system. Below 4.3 K (T^2 = 20 K^2), additional electronic contribution may appear due to defects. Above 6.3 K (T^2 = 40 K^2), upward deviations from the T^3 behavior may be related to low-lying optical modes. For the narrow linear part between 4.3 and 6.3 K we extracted γ = 0.093(5) J/(mole·K^2) that slightly exceeds the calculated value of 0.076 J/(mole·K^2).

Transport Properties. Since single crystals of $Sr_7Cu_{44}As_{23}$ and $Eu_7Cu_{44}As_{23}$ are not available as yet, transport properties were measured on cold-pressed pellets with the highest achievable density and may be affected by grain boundaries. Nevertheless, we were able to establish basic trends in electrical and thermal conductivities of these new compounds. Figure 13 compiles plots of the Seebeck coefficient (S), electrical resistivity (ρ), power factor (PF), and thermal conductivity (κ) for pelletized polycrystalline $A_7Cu_{44}As_{23}$ arsenides between 5 and 395 K. Both compounds exhibit p-type electrical conductivity, with holes being the major carriers. This is indicated by positive values of S in almost entire temperature range. At ambient temperature S amounts to 8.0 μV/K for $Eu_7Cu_{44}As_{23}$ and 6.1 μV/K for $Sr_7Cu_{44}As_{23}$; typical values for compounds with metallic behavior. Indeed, the temperature dependence of the resistivity indicates metallic-type conductivity in agreement with the calculated electronic structure. However, absolute values of the resistivity may be higher than in good metals. We ascribe this effect to the polycrystalline nature of our samples. The upper right inset in Figure 13 shows a kink at $T \approx 17$ K in the resistivity curve for $Eu_7Cu_{44}As_{23}$, which is attributed to the magnetic transition at this temperature. The lower left panel of Figure 13 presents the power factor calculated as PF = S^2/ρ that illustrates the efficiency of charge carrier transport. Although PF is generally low, it rapidly grows with increasing temperature due to the increase in S.

The thermal conductivity of both compounds is fairly low; it does not exceed the value of 1.7 W m^{-1} K^{-1} at the highest temperature reached in our measurements. Using the obtained values of the electrical resistivity, we calculated the tentative electronic contribution (κ_{el}) to the total thermal conductivity (κ) according to the Wiedemann−Franz law $\kappa_{el} = LT/\rho$, where

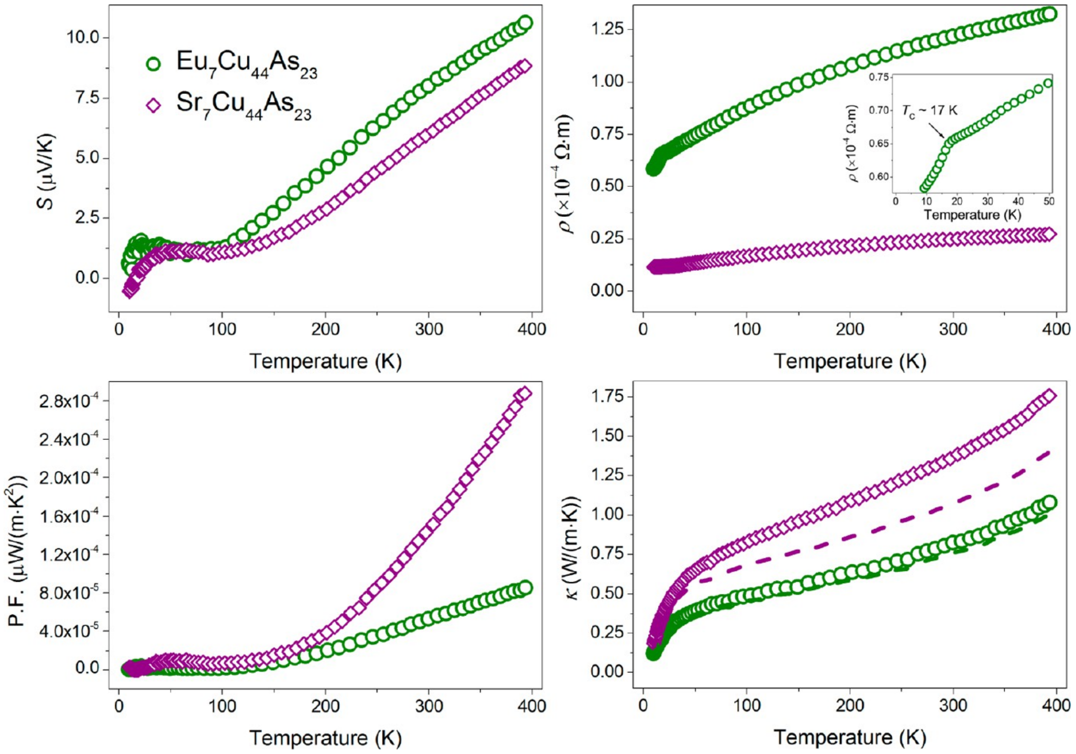

Figure 13. Electronic and heat transport properties of $Eu_7Cu_{44}As_{23}$ (open circles) and $Sr_7Cu_{44}As_{23}$ (◇). Shown are temperature dependencies of the Seebeck coefficient (upper left), electrical resistivity (upper right), power factor (lower left), and thermal conductivity (lower right). The lattice contribution (κ_L) to the thermal conductivity is shown as a dashed line. (inset) The kink of the $Eu_7Cu_{44}As_{23}$ resistivity curve, which is attributed to the ferromagnetic transition at $T \approx 17$ K.

$L = 2.47 \times 10^{-8}$ W Ω K^{-2} is the ideal Lorentz number. Subtracting κ_{el} from κ, we obtained the lattice contribution (κ_L) to the thermal conductivity, which is shown in Figure 13 (lower right) as dashed lines for both $Eu_7Cu_{44}As_{23}$ and $Sr_7Cu_{44}As_{23}$. This suggests that the lattice term provides major contribution to the total thermal conductivity of both samples. We attribute low thermal conductivity to the complexity of the crystal structure. Note however that the overall thermal conductivity as well as the electronic contribution, which is inversely proportional to the experimental resistivity, can be underestimated because of the polycrystalline nature of our samples. Quantitative estimates of the lattice and electronic contributions require transport measurements on single crystals and remain a topic for future studies.

■ CONCLUSIONS

In summary, we have synthesized new arsenides $A_7Cu_{44}As_{23}$ (A = Eu, Sr), which exhibit a crystal structure that can be viewed as a new filled superstructure of $BaHg_{11}$. Cu and As atoms form a 3D framework, with Eu(Sr) atoms adopting the positions of Ba in the parent crystal structure; in addition, Eu(Sr) and As atoms fill the remaining voids in an ordered manner, leading to a 2 × 2 × 2 superstructure of the parent crystal structure. Alternatively, the crystal structure can be viewed as a set of five shells (nested polyhedra) around the A^{2+} cation, where the largest shells are separated by $As[Cu_8]$ cubes and partially interpenetrate each other, resulting in a clathrate-like framework, whose voids are filled by Eu(Sr) and As atoms in an ordered fashion. Magnetization and heat capacity measurements evidence ferromagnetic ordering of the Eu derivative at 17.5 K owing to the alignment of the Eu^{2+} ($4f^7$) centers. Both band structure calculations and transport property measurements show that the new compounds are metals, with low positive values of the Seebeck coefficient. Owing to the complexity of the crystal structure both compounds display low values of thermal conductivity, not exceeding 1.7 W m^{-1} K^{-1} in the range of 5−395 K.

■ ASSOCIATED CONTENT

Ⓢ Supporting Information

X-ray crystallographic files in CIF format. This material is available free of charge via the Internet at http://pubs.acs.org.

■ AUTHOR INFORMATION

Corresponding Authors

*Email: shev@inorg.chem.msu.ru. (A.V.S.)
*E-mail: grin@cpfs.mpg.de. (Y.G.)

Notes

The authors declare no competing financial interest.

■ ACKNOWLEDGMENTS

The authors thank K. Schulze for EDXS analysis. R.D. gratefully acknowledges the Max-Planck Society for a research scholarship. The work in Tallinn has been supported by the Mobilitas program of the ESF (Grant No. MTT77). The research in Moscow was supported in part by the Russian Foundation for Basic Research (Grant No. 13-03-00571) and by the Lomonosov MSU program of development.

■ REFERENCES

(1) Kasper, J. S.; Hagenmuller, P.; Pouchard, M.; Cros, C. *Science* **1965**, *150*, 1713−1714.

(2) Nolas, G. S.; Cohn, J. L.; Slack, G. A.; Schjuman, S. B. *Appl. Phys. Lett.* **1998**, *73*, 178−180.

(3) Paschen, S.; Carrillo-Cabrera, W.; Bentien, A.; Tran, V. H.; Baenitz, M.; Grin, Yu.; Steglich, F. *Phys. Rev. B* **2001**, *64*, 214404.

(4) Sasaki, Y.; Kishimoto, K.; Koyanagi, T.; Asada, H.; Akai, K. *J. Appl. Phys.* **2009**, *105*, 073702.

(5) Zaikina, J. V.; Mori, T.; Kovnir, K.; Teschner, D.; Senyshyn, A.; Schwarz, U.; Grin, Yu.; Shevelkov, A. V. *Chem.—Eur. J.* **2010**, *16*, 12582−12589.

(6) Zhang, H.; Borrmann, H.; Oeschler, N.; Candolfi, C.; Schnelle, W.; Schmidt, M.; Burkhardt, U.; Baitinger, M.; Zhao, J.-T.; Grin, Yu. *Inorg. Chem.* **2011**, *50*, 1250−1257.

(7) Shevelkov, A. V.; Kovnir, K. A. *Struct. Bonding (Berlin, Ger.)* **2011**, *139*, 97−144.

(8) Dubois, F.; Fässler, T. F. *J. Am. Chem. Soc.* **2005**, *127*, 3264−3265.

(9) Aydemir, U.; Akselrud, L.; Carrillo-Cabrera, W.; Candolfi, C.; Oeschler, N.; Baitinger, M.; Steglich, F.; Grin, Yu. *J. Am. Chem. Soc.* **2010**, *132*, 10984−10985.

(10) Kirsanova, M. A.; Olenev, A. V.; Abakumov, A. M.; Bykov, M. A.; Shevelkov, A. V. *Angew. Chem., Int. Ed.* **2011**, *50*, 2371−2374.

(11) Kirsanova, M. A.; Reshetova, L. N.; Olenev, A. V.; Abakumov, A. M.; Shevelkov, A. V. *Chem.—Eur. J.* **2011**, *17*, 5719−5726.

(12) Kirsanova, M. A.; Mori, T.; Maruyama, S.; Matveeva, M.; Batuk, D.; Abakumov, A. M.; Gerasimenko, A. V.; Olenev, A. V.; Grin, Yu.; Shevelkov, A. V. *Inorg. Chem.* **2013**, *52*, 577−588.

(13) Zaikina, J. V.; Kovnir, K. A.; Burkhardt, U.; Schnelle, W.; Haarmann, F.; Schwarz, U.; Grin, Yu.; Shevelkov, A. V. *Inorg. Chem.* **2009**, *48*, 3720−3730.

(14) Fulmer, J.; Lebedev, O. I.; Roddatis, V. V.; Kaseman, D. C.; Sen, S.; Dolyniuk, J. A.; Lee, K.; Olenev, A. V.; Kovnir, K. *J. Am. Chem. Soc.* **2013**, *135*, 12313−12323.

(15) Dünner, J.; Mewis, A. *Z. Anorg. Allg. Chem.* **1995**, *621*, 191−196.

(16) Kovnir, K.; Köhler, U.; Budnyk, S.; Prots, Yu.; Baitinger, M.; Paschen, S.; Shevelkov, A. V.; Grin, Yu. *Inorg. Chem.* **2011**, *50*, 10387−10396.

(17) Kim, S. J.; Ireland, J.; Kannewurf, C. R.; Kanatzidis, M. G. *Chem. Mater.* **2000**, *12*, 3133−3138.

(18) Cordier, G.; Eisenmann, B.; Schäfer, H. *Z. Anorg. Allg. Chem.* **1976**, *426*, 205−214.

(19) Dünner, J.; Mewis, A.; Roepke, M.; Michels, G. *Z. Anorg. Allg. Chem.* **1995**, *621*, 1523−1530.

(20) Frik, L.; Johrendt, D.; Mewis, A. *Z. Anorg. Allg. Chem.* **2006**, *632*, 1514−1517.

(21) Dünner, J.; Mewis, A. *J. Alloys Compd.* **1995**, *221*, 65−69.

(22) Charkin, D. O.; Urmanov, A. V.; Kazakov, S. M.; Batuk, D.; Abakumov, A. M.; Knöner, S.; Gati, E.; Wolf, B.; Lang, M.; Shevelkov, A. V.; Van Tendeloo, G.; Antipov, E. V. *Inorg. Chem.* **2012**, *51*, 8948−8955.

(23) Demchyna, R.; Prots, Yu.; Burkhardt, U.; Schwarz, U. *Book of Abstracts of 16th International Conference on Solid Compound of Transitional Elements;* Max Planck Institute: Germany, 2008 p 257.

(24) Sheldrick, G. M. *Acta Crystallogr.* **2008**, *A64*, 112−122.

(25) *SRM 674a, X-ray Powder Diffraction Institute Sct; National Institute of Standards and Technology;* U.S. Department of Commerce: Gaithersburg, MD, 1989.

(26) Akselrud, L.; Grin, Yu. *J. Appl. Crystallogr.* **2014**, *47*, 803−805.

(27) Koepernik, K.; Eschrig, H. *Phys. Rev. B* **1999**, *59*, 1743−1757.

(28) Perdew, J. P.; Wang, Y. *Phys. Rev. B* **1992**, *45*, 13244−13249.

(29) Blöchl, P. E.; Jepsen, O.; Andersen, O. K. *Phys. Rev. B* **1994**, *49*, 16223−16233.

(30) Peyronel, G. *Gazz. Chim. Ital.* **1952**, *82*, 679−690.

(31) Biehl, K.; Deiseroth, H. J. *Z. Anorg. Allg. Chem.* **1999**, *625*, 1073−1080.

(32) Cordier, G.; Czech, E.; Schäfer, H. *J. Less-Common Met.* **1985**, *108*, 225−239.

(33) Grin, Yu.; Hiebl, K.; Rogl, P.; Godart, C.; Alleno, E. *J. Alloys Compd.* **1997**, *252*, 88−92.

(34) Gladyshevskii, R. E.; Cenzual, K. *J. Alloys Compd.* **1996**, *240*, 266−271.

(35) Lattuner, S. E.; Bilc, D.; Mahanti, S. D.; Kanatzidis, M. G. *Inorg. Chem.* **2009**, *48*, 1346−1355.

(36) Francisco, M. C.; Malliakas, C. D.; Macaluso, R. T.; Prestigiacomo, J.; Haldolaarachchige, N.; Adams, P. W.; Young, D. P.; Jia, Y.; Claus, H.; Gray, K. E.; Kanatzidis, M. G. *J. Am. Chem. Soc.* **2012**, *134*, 12998−13009.

(37) Dietrich, O. W.; Henderson, A. J.; Meyer, H. *Phys. Rev. B* **1975**, *12*, 2844−2855.

(38) McCollum, D. C.; Callaway, J. *Phys. Rev. Lett.* **1962**, *9*, 376−377.

(39) Peierls, R. E. *Quantum Theory of Solids;* Clarendon, Oxford, U.K., 1955.

(40) Bain, G. A.; Berry, J. F. *J. Chem. Educ.* **2008**, *85*, 532−536.